MNE 14 (2022) 100107

Contents lists available at ScienceDirect

Micro and Nano Engineering

journal homepage: www.sciencedirect.com/journal/micro-and-nano-engineering

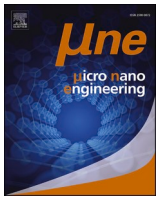

Surface roughness control in nanolaminate coatings of chromium and tungsten nitrides

Marco Beltrami [a,b,*], Simone Dal Zilio [b], Gregor Kapun [c], Catalin Dacian Ciubotaru [b], Federica Rigoni [d], Marco Lazzarino [b], Orfeo Sbaizero [a]

[a] Department of Engineering and Architecture, University of Trieste, 34127 Trieste TS, Italy
[b] CNR-IOM, Istituto Officina dei Materiali - Consiglio Nazionale delle Ricerche, 34149 Trieste TS, Italy
[c] CO-Nanocenter, Center of Excellence on Nanoscience and Nanotechnology, 1000 Ljubljana LJ, Slovenia
[d] Department of Molecular Sciences and Nano-systems, University Ca' Foscari of Venice, 30172 Mestre VE, Italy

ARTICLE INFO

Keywords:
Nanolaminates
Roughness
Hard coatings
Chromium nitride
Tungsten nitride

ABSTRACT

Frictional forces arising during machining operations of cutting tools generate high temperatures at the tool-workpiece interface, promoting tool-wear phenomena. Surface roughness is acknowledged to contribute significantly to friction generation, and its control is therefore of paramount importance. Structural confinement of growth defects in multilayer coating architectures with individual layers thickness in the nanometric regime can help reduce surface roughness development. Here, a set of nanolaminate coatings consisting in an alternated repetition of cubic chromium nitride (CrN) and cubic tungsten nitride (c-WN) layers is fabricated via unbalanced DC magnetron Sputtering. The individual layers thickness range is between 100 and 10 nm. The reduction of surface roughness as a function of individual layers thickness is demonstrated by semi-contact Atomic Force Microscopy (AFM). Scherrer analysis performed on X-Ray Diffraction (XRD) crystallographic signals shows that the reduction in surface roughness is correlated to a reduction in crystallite size, modulated by the nanolaminate architecture. Conformity and uniformity of multilayer coatings is observed via FIB-SEM cross-section micrographs. The relative contribution of CrN and c-WN layers to the overall roughness development is investigated through a SEM cross-section micrograph-based analysis. The microstructural and topographical features of nanostructured CrN/c-WN multilayer coatings are correlated to the observations from the cross-section analysis and discussed in terms of the energy transfer to the growing surface during each deposition step.

1. Introduction

1.1. Tools roughness and friction

Industrial cutting tools such as blades or drill bits are made of High-Speed Steels (HSS) or hard metals, i.e., cermets of tungsten carbide micro-grains embedded in a cobalt or nickel-rich metallic matrix [1]. They are employed in many manufacturing industries, such as automotive, aerospace and wood industries. The lifetime of such tools is limited by the harsh machining conditions, such as high temperatures and abrasive and corrosive wear phenomena, leading to a progressive deterioration of the cutting edge. Eventually, this results in lower surface finishing, increased power consumption, need of parts replacement and ultimately to lower productivity and increased manufacturing costs [1–4]. To extend their service life, cutting tools are usually protected with 2–5 μm of physical vapour deposited (PVD) coatings, consisting of hard and refractory Transition Metal Nitrides (TMNs) such as Titanium Nitride (TiN) and Chromium Nitride (CrN) [5–7]. Although the performance benefits arising from the integration of hard nitride coatings on cutting tools is well consolidated [8], the impact of their low thermal conductivity [9–11] is still open to discussion. Coatings with low thermal conductivity can hardly disperse the frictional heat generated at the tool-workpiece interface towards the tool's body. It has been suggested that this property can be exploited to use coatings as thermal barriers, protecting the underlying tool material from the high interfacial temperatures generated during machining [9]. Nonetheless, this assumes the coating's ability to withstand the harsh environment produced by the simultaneous occurrence of high temperature, oxidizing atmosphere and mechanical forces without being substantially altered. As a matter of fact, the generation and retention of high cutting temperatures deeply

* Corresponding author at: Department of Engineering and Architecture, University of Trieste, 34127 Trieste TS, Italy.
E-mail address: marco.beltrami@phd.units.it (M. Beltrami).

https://doi.org/10.1016/j.mne.2022.100107
Received 21 November 2021; Received in revised form 17 January 2022; Accepted 22 January 2022
Available online 29 January 2022
2590-0072/© 2022 The Author(s). Published by Elsevier B.V. This is an open access article under the CC BY-NC-ND license (http://creativecommons.org/licenses/by-nc-nd/4.0/).

affects the chemical and structural properties of the coatings, ultimately softening and oxidizing the coating material [12–16]. This progressively impairs the mechanical performances of the coatings and compromises the integrity and surface finishing of the workpiece [17,18]. Therefore, heating of the coating surface should be limited as much as possible. Also, the use of lubricants and fluid coolants is starting to be limited, owning to the growing attention to the burden of cooling fluids on the manufacturing economy and on their environmental and health impact [19–22]. Surface roughness plays an important role in friction at the tool-workpiece interface. As a matter of fact, frictional heat arises during machining from the dissipation of shear forces between the two sliding surfaces, which interlock through their surface asperities [23–25]. Roughness in thin films is known to build up with increasing coating thickness [25–27]. Preliminary mechanical treatments or unproper cleaning can leave pre-existing asperities on the substrate. These hinder a conformal coating deposition with the formation of porosities, valleys and ridges whose extent increases with deposition time. Also, different thermal or crystallographic properties between the coating and the substrate material can lead to the establishment of internal stresses in the coating. Eventually, part of the coating material can delaminate or fail, resulting in the creation of voids and ridges on the exposed surface. Accordingly, strategies to diminish the coatings' roughness must be adopted. The integration of multilayer coatings can represent an effective solution to limit the development of surface asperities.

1.2. Nanostructured multilayer coatings

During the last decades, the scientific and industrial interest towards the development of nanostructured multilayer coatings, i.e., nanolaminates, has remarkably grown [3,6,28]. Individual materials lack the complex array of properties required to provide effective protection towards wear sources. The fundamental benefit of using multilayer coatings lies specifically in the possibility to disentangle opposing materials properties, such as hardness and toughness, among the constituent materials [7]. Synergistic effects arise when the thickness of the constituent layers falls in the nanometric regime [21], including enhanced microhardness [29–31], adhesion strength [32,33] and corrosion resistance [34,35] and slower wear rates [28,35,36]. Chromium Nitride is acknowledged as the reference coating material where high temperature oxidation and corrosion are the main sources of wear [17,37–39]. Nonetheless, the mechanical properties of CrN are somewhat lower than other coating materials, with typical microhardness values around 20 GPa for DC-sputtered CrN coatings [29,32,40–43]. For this reason, CrN is often coupled with other nitrides, such as TiN [29,36,44–47], VN [31], MoN [48,49], ZrN [35,43,50,51], NbN [52], AlN [53], and WN [54–57], forming nanolaminate systems with improved mechanical and tribological properties. Among other binary nitrides, tungsten nitride (WN) is known to possess some interesting properties for tribological applications. Monolithic coatings of cubic WN [23,58,59] and nanolaminate systems including cubic WN as one of the constituent materials [60–62] show hardness values typically exceeding 30 GPa and good tribological properties. Besides, when heated in air tungsten nitride forms lubricious oxides characterized by low friction coefficient and abrasive wear rate in dry conditions [63,64]. Despite their low intrinsic hardness [64,65], the formation of such lubricious oxides could be beneficial in the perspective of creating self-lubricant coatings, without the need of external coolant lubricants [24,66,67]. This lubricious behaviour coupled with the opposing antioxidation property of CrN and with the high mechanical properties of cubic WN could yield a composite material with a promising combination of characteristics for tribological applications. Although a few reports on the correlations between surface roughness and wear properties of CrN/WN nanolaminate systems have been previously published, the information about this system is somewhat limited. Firstly, in these studies only coatings with thin bilayer thickness between 30 and 10 nm are considered [54,55]. From a practical and mechanistic point of view, it is interesting to understand which is the threshold at which the nanostructuring benefits arise, and which are the mechanisms behind. More importantly, surface roughness is usually studied only as a final material's property, and it is primarily correlated to the presence and concentration of growth defects [26], with little to no discussion on the contributions of the individual deposition steps to the final roughness level [68]. In the attempt to fill this gap, in this study we have correlated the structural and topographical properties of nanostructured multilayer coatings deposited via DC Magnetron Sputtering and consisting of an alternate sequence of cubic CrN and cubic WN layers, with nominal individual layer thickness varying in the range between 10 and 100 nm. We have also determined the relative contributions of the constituent materials to the final coating's roughness through a cross-section analysis of the nanolaminate coatings. This approach can provide deeper insights in the growth processes and a better control on final coatings properties.

2. Materials and methods

2.1. Samples preparation

Si (100) substrates were cleaned in a two-step process by an ultrasound bath in ethanol (96% pure) for 5 min and RCA-1 solution (H_2O: H_2O_2: NH_4OH at a 3:1:1 ratio in volume) for 10 min at 80 °C, rinsed in deionized water and blow-dried with a nitrogen gun. After the wet-cleaning procedure, substrates were placed in the deposition chamber and pre-treated by Argon - Oxygen plasma cleaning (Ar:O2 ratio of 4:1, working pressure $4*10^{-3}$ mbar, RF power of 100 W). Monolithic and nanolayered coatings were deposited via balanced DC Magnetron Sputtering in reactive mode. Substrate to target distance was 8 cm. A negative substrate bias of -40 V was applied to the substrates by means of an external DC generator and substrates were heated to 200 °C, to ensure a good film adhesion and low porosity. An interlayer of 75 ± 9 nm of metallic Cr was deposited in each process prior than the multilayer coatings to improve the adhesion to the Si substrates. The deposition of nitride coatings was accomplished by a DC Reactive Sputtering procedure using 6-in. target of metallic Cr (99.995%) and W (99.95%) in a nitrogen and argon reactive gas mixture. CrN layers were deposited at a N_2 sccm fraction of 66% with a Cr target power density of 2.7 W cm^{-2}, while WN layers were obtained by introducing a gas mixture consisting of a N_2 sccm fraction of 35% with a target power density of 1.6 W cm^{-2}. In both cases, the working pressure was regulated to 3.0 ± 0.1 * 10^{-3} mbar. In such conditions, deposition rates were 0.74 nm/s and 0.72 nm/s for CrN and WN layers respectively, as measured in separate calibration experiments via FIB cross-section imaging on single layers test coatings. In all the samples, the first nitride layer being deposited was CrN and the total coating thickness was controlled to 1.2 ± 0.1 μm to exclude any relevant thickness dependence on coatings roughness.

2.2. XRD characterization

X-Ray diffraction data were collected using a powder-diffractometer Bruker-AXS Siemens D5005 (Bruker, Billerica, Massachusetts, USA) mounting a monochromatized Cu radiation source and a 2-mm convergence slid. XRD theta-2theta scans were run in a conventional Bragg-Brentano arrangement, with 2θ values ranging between 20 and 50 degrees at steps of 0.05 degrees and an acquisition time of 10 s per point. Scherrer analysis was used for the determination of the crystallite's apparent size in nanolaminates. Any additional contributions to the width of the diffraction peaks besides the crystallite size, such as instrumental effects and micro-strain [69], were not considered. More details are included in Section 3 of the Supplementary Information file.

2.3. AFM characterization

AFM measurements were run in semi-contact mode on an Asylum

Research MFP3D AFM probe (Oxford Instruments, Abingdon, England) using diamond-like carbon (DLC) non-contact NSG01 tips with a nominal tip-curvature radius of 2 nm (NT-MDT®, NT-MDT LLC, Moscow - Zelenograd, Russia). For each sample, five 5-μm-square surface areas were imaged, from which average and standard deviation data were calculated through Gwydion™ software.

2.4. SEM-FIB cross-section imaging

FIB cross-sections on multilayer samples were fabricated using FIB-SEM Helios Nanolab 650 (Thermo Fisher Scientific, The Netherlands), equipped with X-Max 50 SDD EDX detector (Oxford, UK). First, as-deposited samples were covered with a protective 700-nm thick platinum layer via e-beam evaporation by introducing a metalorganic precursor. Subsequently, fine cross-sections were cut by progressively reducing the ion-beam current of the FIB from 2.5 nA to 0.4 nA at 30 kV. Eventually, clean cross-sections were imaged via low kV SEM approach (2 kV at 13 pA) at a tilt angle of 38° in respect to the samples surface normal. Cross sections images were analyzed via a home-made script in MATLAB® (The MathWorks, Massachusetts, USA). Details on the procedure can be found in the Supplementary Information to this paper, in Section 2. Briefly, taking advantage of the different *Z*-contrast between W-rich layers and Cr-rich layers, the differential variation profile of pixel values across each image vertical line was used to identify the location of each interface. The procedure was repeated to identify all the interfacial profiles across the whole cross-section images. The standard deviation *Std* of each interface profile was then calculated. This value represents the deviation of each profile from perfect linearity; hence, it is correlated to the roughness of the interface upon which the curve was determined. Finally, the relative variation $r_{1/2}$ of interfacial roughness-related *Std* values for two subsequent interfaces (i.e., belonging to a different order, namely CrN-on-WN or WN-on-CrN) was calculated as

$$r_{1/2} = \frac{Std_1^i - Std_2^{i-1}}{Std_2^{i-1}} * 100$$

Subscripts 1 and 2 refer respectively to the topmost and underlying interfaces in each pair and i is the interface position index. The $r_{1/2}$ values were calculated for all the interface pairs from the coating's surface towards the Cr interlayer. Then, the whole set of $r_{1/2}$ values was separated into distinct CrN-on-WN and WN-on-CrN series, with the $r_{1/2}$ values constituting each series defined as ${r_{1/2}}^{CrN/WN}$ and ${r_{1/2}}^{WN/CrN}$ respectively. The corresponding mean values $<{r_{1/2}}^{CrN/WN}>$ and $<{r_{1/2}}^{WN/CrN}>$ were then calculated for each cross-section image by averaging the ${r_{1/2}}^{CrN/WN}$ and ${r_{1/2}}^{WN/CrN}$ series separately. At least three cross-sections per multilayer architecture were processed according to the procedure descripted above, each providing one $<{r_{1/2}}^{CrN/WN}>$and one $<{r_{1/2}}^{WN/CrN}>$ values. These were eventually used to calculate the architecture-average values $<{R_{1/2}}^{CrN/WN}>$and $<{R_{1/2}}^{WN/CrN}>$ for each coating architecture.

3. Results

3.1. XRD characterization

Depending on deposition parameters such as reactive gas mixture composition, substrate bias and substrate temperature, tungsten and chromium nitrides can be deposited in cubic phases, hexagonal phases or a mixture of the two [58,70]. By comparing the diffraction data, the averages of which are reported in Fig. 1, with the Powder Diffraction File (PDF) database, both CrN and WN are found to be deposited in their cubic phases, with a dominating (200) orientation. Concerning CrN, (111) and (200) peaks occur respectively at 2θ values of 37.4 and 43.6 degrees, whilst for cubic WN, the same peaks occur at 37.1 and 42.8 degrees respectively. The peak occurring at 2θ value of 33.35 is attributed to the 1st order forbidden Si (200) reflection coming from the substrate [71]. For completion, we mention that broader and less intense peaks were also observed at angular positions of around 63 and 75 degrees, attributed respectively to the (220) and (311) reflections of the nitride cubic phases of CrN and WN [70] (data not shown). A more thorough dissertation on the phase identification of CrN and c-WN is given in Section 1 in the Supplementary Information. Briefly, by comparing the diffraction data with an Energy Dispersive X-Ray (EDX) chemical analysis, we stated that CrN coatings consist of a stoichiometric cubic CrN phase, while c-WN consist of a non-stoichiometric cubic phase with a nitrogen atomic fraction of 45.2% at., just in the middle between the predicted values for the pure cubic β-W_2N and c-W_3N_4 phases, respectively 33.3% at. and 57.2% at. In nanolaminate systems the cubic phases are retained while peak maximum positions and intensities vary in respect to the monolithic references and among the different multilayer architectures. The apparent crystallite sizes are calculated by performing Scherrer analysis on the nanolaminates (200) peak signals. First, nanolaminate (200) signals are deconvoluted into their CrN (200) and WN (200) components, using Voigt curves to fit the experimental profiles. Then, the full width at half maximum (FWHM) value and peak maximum position θ of each component's peak were used in the Scherrer Eq. [72]:

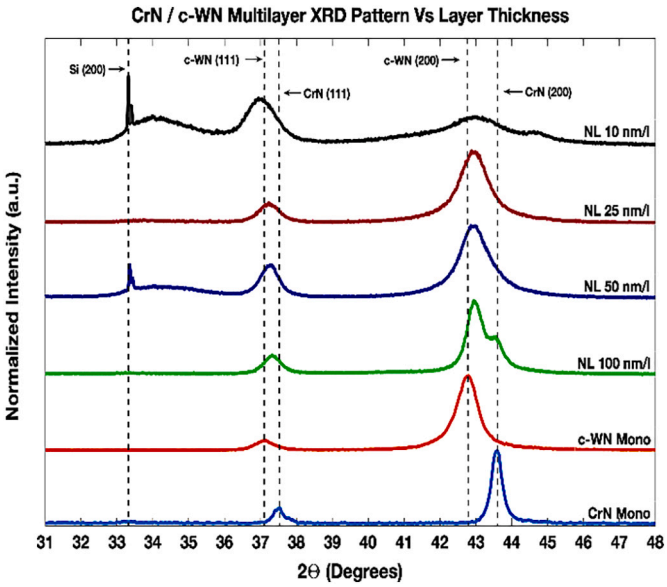

Fig. 1. Normalized XRD plots of monolithic and nanolaminate (NL) coatings. Peak indices reported next to the corresponding peak positions are referred to the peak position of the monolithic coatings.

$$D_{hkl} = K^* \frac{\lambda}{FWHM_{hkl} * cos\theta_{hkl}}$$

Where D is the crystallite size, λ is the x-ray wavelength (0.15414 nm for Cu Kα radiation), *hkl* are the Miller indices of the analyzed peak (h = 2, k = l = 0 in the present case), and K is the Scherrer shape-factor coefficient, set equal to 0.9 by convention, detailed crystallites shape information being missing [72,73].

The results of the Scherrer analysis are summarized in Fig. 2 for all the coating systems investigated. All coating systems are found to be nanocrystalline and crystallite size decreases by downscaling the individual layers thickness, with a similar trend for CrN and c-WN crystallites.

3.2. AFM characterization

The extent of surface roughness has been analyzed via semi-contact atomic force microscopy. In Fig. 3, selected bidimensional 5-um square AFM topographies of monolithic c-CrN and c-WN as well as of

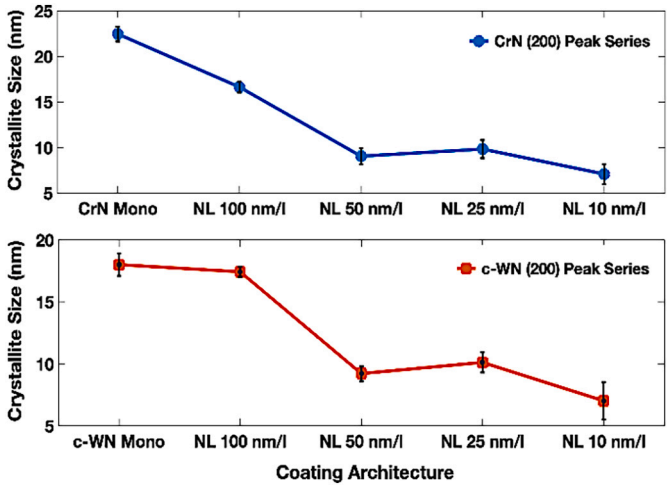

Fig. 2. Crystallite sizes of monolithic and nanolaminate (NL) CrN/c-WN coatings calculated by applying the Scherrer equation on fitted CrN and c-WN (200) peaks.

nanolaminate (NL) samples with 100 nm/layer and 10 nm/layer architecture are shown. All the surfaces are homogeneous with roughness values in the nanometer regime. As shown in Fig. 4, Monolithic CrN expressed the highest roughness value among all coatings, while monolithic c-WN coatings comparatively showed a noticeably low roughness. The surface roughness of multilayer coatings is shown to decrease with decreasing individual layers thickness. This is in good agreement with the general assumption that the lower the deposition time for each constituent layer, i.e., its thickness, the lower the building up of structural defects such as porosities and piling up of coating material.

3.3. FIB-SEM cross-section analysis

Surface roughness in thin films is primarily due to the formation of structural and topographical defects during the deposition process [25,26]. By replacing a continuous deposition with a stepwise deposition of alternating materials, the growth of such defects is reduced thanks to materials discontinuity and limited by the individual layers thickness. A representative FIB-cut Cross-Section SEM image of a CrN/c-WN multilayer coating with an individual layer thickness of 25 nm is illustrated in Fig. 5. A representative set of samples spanning the whole range of individual layer thickness treated in this study is illustrated in the Supplementary Information file, section 1.1.2. In all cases, the coatings are conformal and no major defects such as microparticles or

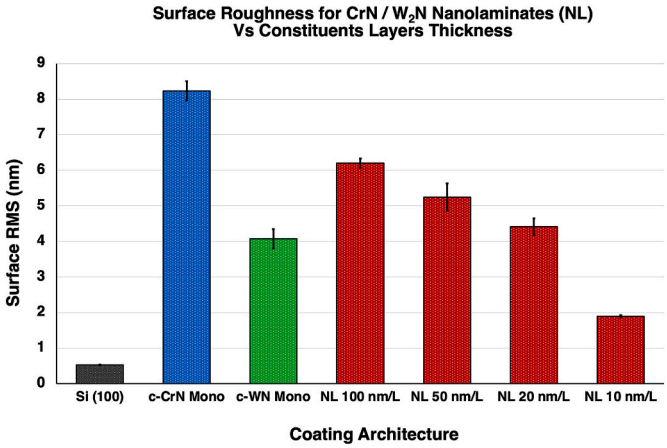

Fig. 4. RMS values of surface roughness for monolithic and multilayer coatings. The surface roughness of bare Si (100) substrate is reported for completion. Error bars represent standard deviations of measured RMS values.

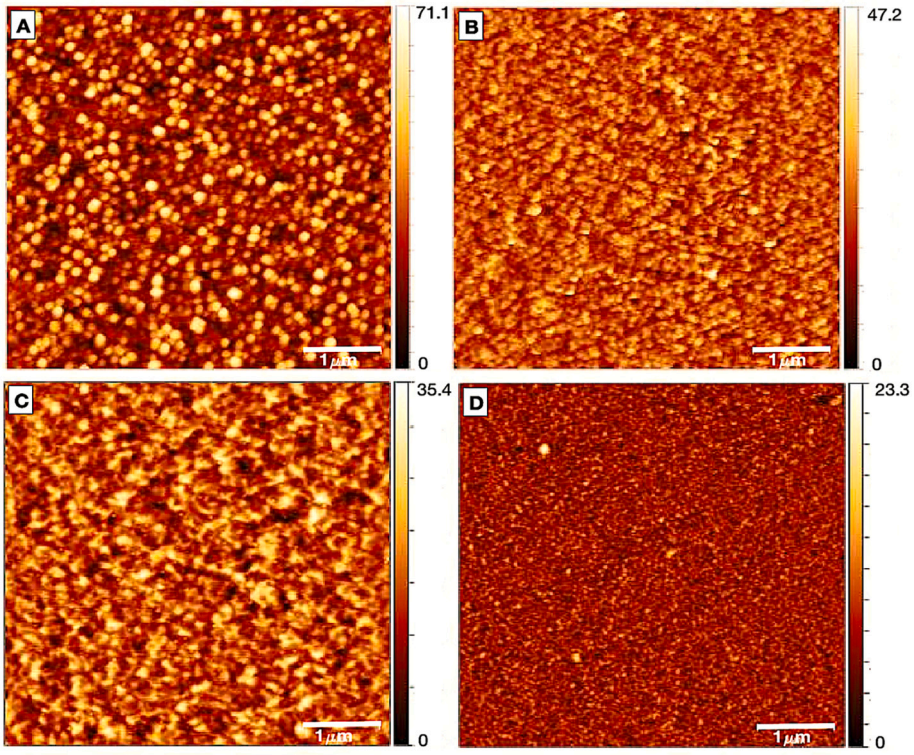

Fig. 3. 2D AFM topographies of monolithic (A) CrN and (B) c-WN, Multilayer CrN/WN with individual layer thickness of 100 nm (C) and 10 nm (D) respectively. Colour-bars represent the maximum peak-to-trough distance.

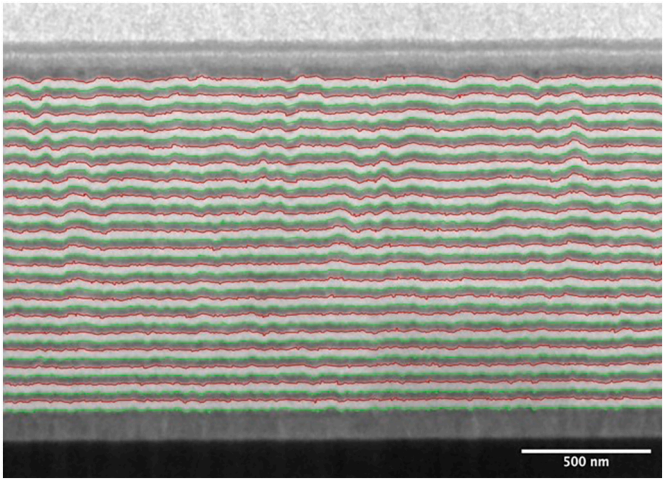

Fig. 5. FIB-SEM cross section image of a nominal 25 nm/l sample. Interlayer profiles are highlighted, with red and green lines for c-WN and CrN upper interface respectively. (For interpretation of the references to colour in this figure legend, the reader is referred to the web version of this article.)

cavities are visible. The interlayer roughness builds up with subsequent deposition steps (see Section 1.1.3 in the Supplementary Information). Despite this general trend, further insights can be achieved by analysing the relative contribution of the two constituent layers to the overall roughness development. The comprehensive results of such analysis are reported in Fig. 6 for each nanolaminate architecture. Here, the architecture-average $<R_{1/2}{}^{CrN/WN}>$and $<R_{1/2}{}^{WN/CrN}>$values, defined in Section 2.4, are reported. The two materials behave differently. Apparently, while WN layers contribute positively to the overall roughness in all nanolaminate systems, the effect of CrN layers seems to be more complex, as discussed in the following section. For both series, the corresponding effect is larger when relatively thick layers are deposited and decreases with the individual layers thickness.

4. Discussion

Nanolaminate coatings based on alternating CrN and c-WN showed a decreasing surface roughness with progressively thinner constituent layers (Fig. 4). This could be explained by considering a reduction of deposition topological defects such as porosities, asperities, and particles inclusions. Nonetheless, FIB-cut SEM cross section images show that all the nanolaminates are conformal (see Fig. 5 and Fig. 2.2 included in the Section 2 of the Supplementary Information), and AFM topographies show homogenous surfaces with just a few particles inclusions (Fig. 3).

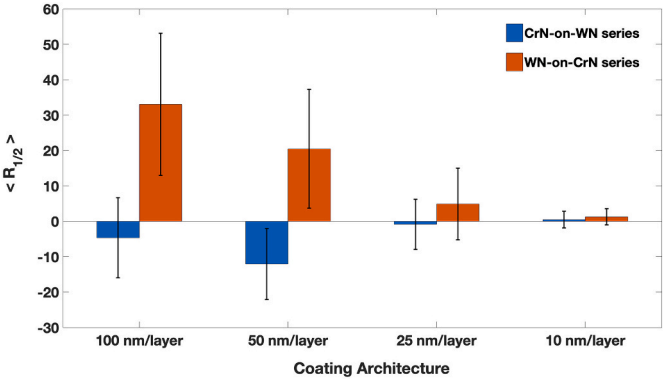

Fig. 6. Comparison of the architecture-averaged $<R_{1/2}{}^{CrN/WN}>$and $<R_{1/2}{}^{WN/CrN}>$values, as defined in Section 2.4, for all the coatings architectures considered, with the corresponding standard deviations.

Hence, the origin of surface roughness is hardly due to particles inclusions or non-conformal deposition. It is then possible to assume that the surface asperities visible in the SEM cross-sections could originate from growth processes of misoriented crystals during coating deposition. The XRD data reported in Fig. 1 and the results of the Scherrer analysis in Fig. 2 show that all the coatings are polycrystalline with grain sizes on the order of 20 to 7 nm for architectures with progressively thinner constituent layers. These values are of the same order of magnitude of the roughness values found in the AFM analysis. The stepwise alternated deposition of two different materials allows to periodically block the crystal growth processes, yielding a finer grain-size. With a finer grain size, the volume fraction of amorphous interface region increases accordingly. This can contribute to the achievement of a lower roughness for as-deposited coatings. Indeed, the increased volume of amorphous material imposes fewer directional growth constraints than in coarser-grained structures. Consequently, asperities due to misoriented grains are effectively reduced. Therefore, the distance between two consecutive interfaces constitutes an upper bound for crystallites volume and this size-confinement effect is then probably responsible for the reduced surface roughness in nanolaminate coatings. Interestingly, we found that the situation is more complex, as the two constituent layers contribute differently. In all the investigated systems, the average contribution of c-WN layers to the roughness development, represented by the $<R_{1/2}{}^{WN/CrN}>$value, is positive. This means that each new c-WN layer adds asperities to the growing film. On the contrary, except for the coating system with the thinner constituent layers, the contribution of CrN, represented by the $<R_{1/2}{}^{CrN/WN}>$value, is negative. This suggests each new CrN layer apparently reabsorbs some of the pre-existing asperities. As shown in Fig. 6, the magnitude of the two materials' contribution evolves differently as a function of the individual layers thickness. The magnitude of $<R_{1/2}{}^{WN/CrN}>$decreases monotonically with the individual layers thickness, and such behaviour can be rationalized by considering a size-confinement effect [55]; on the contrary, the evolution of $<R_{1/2}{}^{CrN/WN}>$shows a different trend, requiring a more insightful description. Despite the AFM analysis showed that monolithic CrN develops a higher roughness than monolithic c-WN (Fig. 4), it contributes less to the overall roughness development in nanolaminate systems. This behaviour can be explained by considering the energy transfer contributions to the growing surface during WN and CrN deposition steps [74–80]. In sputtering processes with a negatively biased substrate, the energy delivered to the growing surface is largely constituted by the kinetic energy of impinging positive ions accelerated through the substrate sheath [78] and the flux of reflected neutrals [78,80] and only marginally on the input target power [76]. The sputtering yield depends on the relative atomic weight of target atoms and gas ions [75,78,80]. Hence, due to the larger target-to-argon atomic weight ratio, the sputtering yield of tungsten in argon plasma is less than that of chromium. This results in the ejection of fewer metallic ions and atoms but with higher kinetic energy in the case of Tungsten sputtering than with Chromium sputtering [75]. Also. the larger target-to-mass ratio enhances the backscattering efficiency of neutralized Argon atoms at the target surface towards the growing film [75]. Besides, the higher Ar fraction (65% vs 33%) and the lower target power densities (2.7 vs 1.6 W*cm^{-2}) used during the deposition of WN layers further increase the density of backscattered Ar atoms [77,81]. Therefore, more energetic particles and more neutralized Ar atoms impinge on the growing surface during the deposition of WN layers. Both these contributions can explain the levelling of the underlying CrN layers during WN deposition steps as well as the absence of the same effect when depositing CrN on the previous WN layers. These two effects are somewhat counter balanced by the higher tendency of CrN to form rough surfaces, as AFM analysis showed in Fig. 3. Hence, it can be assumed that when the individual layer thickness is still relatively high, as in the case of samples with 100 nm/l architecture, the surface-levelling effect described earlier is opposed by the intrinsic roughness development behaviour. When the individual layer thickness is brought

down to 50 nm/l and thinner, the second contribution is constrained, allowing a more pronounced roughness reduction effect. As the constituent layers thickness is further reduced to 25 nm per layer, the two opposing trends of CrN and c-WN are still retained, but with a much lower magnitude. Eventually, as the individual layer thickness is restricted to 10 nm per layer, both contributions substantially approach zero owning to the very thin constituent layers. As a matter of facts, a slight trend inversion seems to occur. This fact might be explained by considering the relative nature of the roughness variations. In fact, by reducing the thickness of the individual layers, the positive roughness variation carried by c-WN layers is almost annihilated, and the relative negative contribution carried by CrN might then look reversed.

5. Conclusions

In this work the development of roughness in nanolaminate coatings consisting of alternated CrN and cubic WN layers deposited via reactive magnetron sputtering has been studied in respect to structural, topographical and design considerations. Nanostructured multilayer coatings are found to be nanocrystalline and to retain the crystallographic features of the individual materials. Nanostructured multilayer coatings show a reduced surface roughness than monolithic CrN, the difference being enhanced with reducing the constituent layers thickness. The contributions of the two constituent materials to the roughness build up is investigated and discussed for all the multilayer systems considered. We found that the two materials behave in opposing manner, with c-WN upper interfaces positively contributing to the overall roughness development and CrN upper interfaces partly recovering the surface irregularities of the underlying interface. The validity of this layer-by-layer characterization route can be of use not only in tribological coatings but in any deposition route of multilayer materials where surface roughness control is important, for instance for barrier coatings and reflective mirrors. Further studies are then required to verify this anisotropic behaviour for other multilayer systems, to clearly establish relations between materials intrinsic characteristics and deposition design routes.

Declaration of Competing Interest

The authors declare no conflict of interests.

Acknowledgments

This research project was entirely funded by the NANO-REGION project under the ITA-SLO Interreg program.

We thank Dr. Davide Cristofori (DSMN, University Ca' Foscari of Venice) for his contribution in the SEM-EDX analysis.

Appendix A. Supplementary data

Supplementary data to this article can be found online at https://doi.org/10.1016/j.mne.2022.100107.

References

[1] A. Rizzo, et al., The critical raw materials in cutting tools for machining applications: a review, Materials (Basel). 13 (6) (2020) 1–49.
[2] J. Karandikar, T. McLeay, S. Turner, T. Schmitz, Tool wear monitoring using naïve Bayes classifiers, Int. J. Adv. Manuf. Technol. 77 (9–12) (2015) 1613–1626.
[3] H. Caliskan, P. Panjan, C. Kurbanoglu, Hard Coatings on Cutting Tools and Surface Finish vol. 3–3, Elsevier Ltd, 2017 no. January 2017.
[4] A. Naylor, P. Hackney, A review of wood machining literature with a special focus on sawing, BioResources 8 (2) (2013) 3122–3135.
[5] H. Caliskan, P. Panjan, C. Kurbanoglu, Hard coatings on cutting tools and surface finish, Compr. Mater. Finish. 3–3 (June) (2017) 230–242.
[6] B. Navinšek, P. Panjan, I. Milošev, PVD coatings as an environmentally clean alternative to electroplating and electroless processes, Surf. Coat. Technol. 116–119 (1999) 476–487.
[7] A. Pogrebnjak, K. Smyrnova, O. Bondar, Nanocomposite multilayer binary nitride coatings based on transition and refractory metals: structure and properties, Coatings 9 (3) (2019).
[8] D.T. Quinto, Twenty-five years of pvd coatings at the cutting edge, News Bull. A Publ. Vac. Coat. Ind. 5 (20) (2007) 17–22.
[9] M.K. Samani, et al., Thermal conductivity of titanium nitride/titanium aluminum nitride multilayer coatings deposited by lateral rotating cathode arc, Thin Solid Films 578 (2015) (2015) 133–138.
[10] M.A. Gharavi, et al., Microstructure and thermoelectric properties of CrN and CrN/Cr2N thin films, J. Phys. B Appl. Phys. 51 (35) (2018) 35–53.
[11] K. Jagannadham, Thermal conductivity of nitride films of Ti, Cr, and W deposited by reactive magnetron sputtering, J. Vac. Sci. Technol. A Vacuum, Surfaces, Film. 33 (3) (2015), 031514.
[12] L. Hultman, Thermal stability of nitride thin films, Vacuum 57 (1) (2000) 1–30.
[13] H.C. Barshilia, K.S. Rajam, Raman spectroscopy studies on the thermal stability of TiN, CrN, TiAlN coatings and nanolayered TiN/CrN, TiAlN/CrN multilayer coatings, J. Mater. Res. 19 (11) (2004) 3196–3205.
[14] Y.G. Shen, Y.W. Mai, W.E. McBride, Q.C. Zhang, D.R. McKenzie, Structural properties and nitrogen-loss characteristics in sputtered tungsten nitride films, Thin Solid Films 372 (1) (2000) 257–264.
[15] H. Lind, et al., Improving thermal stability of hard coating films via a concept of multicomponent alloying, Appl. Phys. Lett. 99 (9) (2011) 2011–2014.
[16] C.C. Kuo, Y.T. Lin, A. Chan, J.T. Chang, High temperature wear behavior of titanium nitride coating deposited using high power impulse magnetron sputtering, Coatings 9 (9) (2019) 1–13.
[17] P. Panjan, B. Navinšek, A. Cvelbar, A. Zalar, I. Milošev, Oxidation of TiN, ZrN, TiZrN, CrN, TiCrN and TiN/CrN multilayer hard coatings reactively sputtered at low temperature, Thin Solid Films 281–282 (1–2) (1996) 298–301.
[18] I. Horman, I. Busuladžic, E. Azemovic, Temperature influence on wear characteristics and blunting of the tool in continuous wood cutting process, Proc. Eng. 69 (2014) 133–140.
[19] E. Benedicto, D. Carou, E.M. Rubio, Technical, economic and environmental review of the lubrication/cooling systems used in machining processes, Proc. Eng. 184 (2017) 99–116.
[20] N.R. Dhar, M. Kamruzzaman, M. Ahmed, Effect of minimum quantity lubrication (MQL) on tool wear and surface roughness in turning AISI-4340 steel, J. Mater. Process. Technol. 172 (2) (2006) 299–304.
[21] G.S. Goindi, P. Sarkar, Dry machining: a step towards sustainable machining – challenges and future directions, J. Clean. Prod. 165 (2017) 1557–1571.
[22] N.R. Dhar, M. Kamruzzaman, Cutting temperature, tool wear, surface roughness and dimensional deviation in turning AISI-4037 steel under cryogenic condition, Int. J. Mach. Tools Manuf. 47, no. 5 SPEC. ISS (2007) 754–759.
[23] T. Polcar, N.M.G. Parreira, A. Cavaleiro, Structural and tribological characterization of tungsten nitride coatings at elevated temperature, Wear 265 (3–4) (2008) 319–326.
[24] M. Woydt, A. Skopp, I. Dörfel, K. Witke, Wear engineering oxides/antiwear oxides©, Tribol. Trans. 42 (1) (1999) 21–31.
[25] P. Panjan, A. Drnovšek, P. Gselman, M. Čekada, M. Panjan, Review of growth defects in thin films prepared by PVD techniques, Coatings 10 (5) (2020).
[26] P. Panjan, M. Čekada, M. Panjan, D. Kek-Merl, Growth defects in PVD hard coatings, Vacuum 84 (1) (2009) 209–214.
[27] D.M. Mattox, Surface effects on the growth, adhesion and properties of reactively deposited hard coatings, Surf. Coat. Technol. 81 (1) (1996) 8–16.
[28] A. Krella, Resistance of PVD coatings to erosive and wear processes: a review, Coatings 10 (10) (2020).
[29] A. Azizpour, R. Hahn, F.F. Klimashin, T. Wojcik, E. Poursaeidi, Deformation and cracking mechanism in CrN / TiN multilayer coatings, Coatings 9 (363) (2019) 9–17.
[30] R. Bendikiene, E. Pupelis, Application of surfaced cutters for machining of wood-based materials, Wood Res. 61 (1) (2016) 155–162.
[31] Y. Qiu, et al., Improvement of tribological performance of CrN coating via multilayering with VN, Surf. Coat. Technol. 231 (2013) 357–363.
[32] J.J. Roa, et al., Contact damage and fracture micromechanisms of multilayered TiN/CrN coatings at micro- and nano-length scales, Thin Solid Films 571 (P2) (2014) 308–315.
[33] A. Gilewicz, B. Warcholinski, Tribological properties of CrCN/CrN multilayer coatings, Tribol. Int. 80 (2014) 34–40.
[34] C. Gaona-Tiburcio, et al., Corrosion resistance of multilayer coatings deposited by PVD on Inconel 718 using electrochemical impedance spectroscopy technique, Coatings 10 (6) (2020) 1–11.
[35] P.M. Samim, A. Fattah-alhosseini, H. Elmkhah, O. Imantalab, Nanoscale architecture of ZrN/CrN coatings: microstructure, composition, mechanical properties and electrochemical behavior, J. Mater. Res. Technol. 15 (2021) 542–560.
[36] E. Lotfi-khojasteh, M. Sahebazamani, H. Elmkhah, M. Nouri, O. Imantalab, A. Fattah-alhosseini, A study of the electrochemical and tribological properties of TiN/CrN nano-layer coating deposited on carburized-H13 hot-work steel by Arc-PVD technique, J. Asian Ceram. Soc. 9 (1) (2021) 247–259.
[37] B. Navinšek, P. Panjan, I. Milošev, Industrial applications of CrN (PVD) coatings, deposited at high and low temperatures, Surf. Coat. Technol. 97 (1–3) (1997) 182–191.
[38] B. Navinšek, P. Panjan, A. Cvelbar, Characterization of low temperature CrN and TiN (PVD) hard coatings, Surf. Coat. Technol. 75 (1995) 155–161.
[39] K. Jokar, H. Elmkhah, A. Fattah-Alhosseini, K. Babaei, A. Zolriasatein, Comparison of the wear and corrosion behavior between CrN and AlCrN coatings deposited by arc-PVD method, Mater. Res. Exp. 6 (11) (2019), 116426.

[40] Q. Wang, F. Zhou, J. Yan, Evaluating mechanical properties and crack resistance of CrN, CrTiN, CrAlN and CrTiAlN coatings by nanoindentation and scratch tests, Surf. Coat. Technol. 285 (2016) 203–213.
[41] E.Y. Choi, M.C. Kang, D.H. Kwon, D.W. Shin, K.H. Kim, Comparative studies on microstructure and mechanical properties of CrN, Cr-C-N and Cr-Mo-N coatings, J. Mater. Process. Technol. 187–188 (2007) 566–570.
[42] B. Warcholinski, A. Gilewicz, Tribological properties of CrNx coatings, J. Ach. Mater. Manuf. Eng. 47 (2) (2009) 498–504.
[43] O.V. Maksakova, et al., Nanoscale architecture of (CrN/ZrN)/(Cr/Zr) nanocomposite coatings: microstructure, composition, mechanical properties and first-principles calculations, J. Alloys Compd. 831 (2020).
[44] J.W. Du, L. Chen, J. Chen, Y. Du, Mechanical properties, thermal stability and oxidation resistance of TiN/CrN multilayer coatings, Vacuum 179 (2020), 109468.
[45] Z.A. Fazel, H. Elmkhah, A. Fattah-Alhosseini, K. Babaei, M. Meghdari, Comparing electrochemical behavior of applied CrN/TiN nanoscale multilayer and TiN single-layer coatings deposited by CAE-PVD method, J. Asian Ceram. Soc. 8 (2) (2020) 510–518.
[46] N.S. Mansoor, A. Fattah-Alhosseini, H. Elmkhah, A. Shishehian, Comparison of the mechanical properties and electrochemical behavior of TiN and CrN single-layer and CrN/TiN multi-layer coatings deposited by PVD method on a dental alloy, Mater. Res. Exp. 6 (12) (2019), 126433.
[47] N.S. Mansoor, A. Fattah-alhosseini, H. Elmkhah, A. Shishehian, Electrochemical behavior of TiN, CrN and TiN/CrN nanostructured coatings on the nickel-chromium alloy used in dental fixed prosthesis, J. Asian Ceram. Soc. 8 (3) (2020) 694–710.
[48] B.O. Postolnyi, et al., Multilayer design of CrN / MoN protective coatings for enhanced hardness and toughness, J. Alloys Compd. 725 (2017) 1188–1198.
[49] A.D. Pogrebnjak, et al., Superhard CrN/MoN coatings with multilayer architecture, Mater. Des. 153 (2017) (2018) 47–59.
[50] P. Mohamadian Samim, A. Fattah-Alhosseini, H. Elmkhah, O. Imantalab, Structure and corrosion behavior of ZrN/CrN nano-multilayer coating deposited on AISI 304 stainless steel by CAE-PVD technique, J. Asian Ceram. Soc. 8 (2) (2020) 460–469.
[51] P.M. Samim, A. Fattah-alhosseini, H. Elmkhah, O. Imantalab, M. Nouri, A study on comparing surface characterization and electrochemical properties of single-layer CrN coating with nanostructured multilayer ZrN/CrN coating in 3.5 wt.% NaCl solution, Surf. Interf. 21 (September) (2020).
[52] Y.P. Purandare, A.P. Ehiasarian, P.E. Hovsepian, Deposition of nanoscale multilayer CrN/NbN physical vapor deposition coatings by high power impulse magnetron sputtering, J. Vac. Sci. Technol. A Vacuum, Surfaces, Film. 26 (2) (2008) 288–296.
[53] J. Lin, J.J. Moore, B. Mishra, M. Pinkas, W.D. Sproul, Nano-structured CrN/AlN multilayer coatings synthesized by pulsed closed field unbalanced magnetron sputtering, Surf. Coat. Technol. 204 (6–7) (2009) 936–940.
[54] Y.Z. Tsai, J.G. Duh, Tribological behavior of CrN/WN multilayer coatings grown by ion-beam assisted deposition, Surf. Coat. Technol. 201 (7 SPEC. ISS) (2006) 4266–4272.
[55] F.B. Wu, S.K. Tien, J.G. Duh, Manufacture, microstructure and mechanical properties of CrWN and CrN/WN nanolayered coatings, Surf. Coat. Technol. 200 (5–6) (2005) 1514–1518.
[56] P. Hones, R. Consiglio, N. Randall, F. Leacutevy, Mechanical properties of hard chromium tungsten nitride coatings, Surf. Coat. Technol. 125 (1–3) (2000) 179–184.
[57] W.Y. Wu, et al., Microstructure, mechanical and tribological properties of CrWN films deposited by DC magnetron sputtering, Vacuum 87 (2013) 209–212.
[58] P. Hones, N. Martin, M. Regula, F. Lévy, Structural and mechanical properties of chromium nitride, molybdenum nitride, and tungsten nitride thin films, J. Phys. D. Appl. Phys. 36 (8) (2003) 1023–1029.
[59] T. Polcar, N.M.G. Parreira, A. Cavaleiro, Tribological characterization of tungsten nitride coatings deposited by reactive magnetron sputtering, Wear 262 (2007) 655–665.
[60] J. Buchinger, et al., Toughness enhancement in TiN/WN superlattice thin films, Acta Mater. 172 (June) (2019) 18–29.
[61] A.A. Bagdasaryan, et al., Structural and mechanical characterization of (TiZrNbHfTa)N/WN multilayered nitride coatings, Mater. Lett. 229 (2018) 364–367.
[62] D.D. Kumar, N. Kumar, S. Kalaiselvam, S. Dash, R. Jayavel, Wear resistant super-hard multilayer transition metal-nitride coatings, Surf. Interf. 7 (March) (2017) 74–82.
[63] G. Gassner, P.H. Mayrhofer, K. Kutschej, C. Mitterer, M. Kathrein, Magnéli phase formation of PVD Mo-N and W-N coatings, Surf. Coat. Technol. 201 (6) (2006) 3335–3341.
[64] T. Polcar, N.M.G. Parreira, A. Cavaleiro, Tungsten oxide with different oxygen contents: sliding properties, Vacuum 81 (11–12) (2007) 1426–1429.
[65] N.M.G. Parreira, N.J.M. Carvalho, A. Cavaleiro, Synthesis, structural and mechanical characterization of sputtered tungsten oxide coatings, Thin Solid Films 510 (1–2) (2006) 191–196.
[66] G. Gassner, P.H. Mayrhofer, K. Kutschej, C. Mitterer, M. Kathrein, A new low friction concept for high temperatures: lubricious oxide formation on sputtered VN coatings, Tribol. Lett. 17 (4) (2004) 751–756.
[67] D. Wainstein, A. Kovalev, Tribooxidation as a way to improve thewear resistance of cutting tools, Coatings 8 (6) (2018) 1–9.
[68] D.G. Stearns, P. Mirkarimi, E. Spiller, Localized defects in multilayer coatings, Thin Solid Films 446 (2004) 37–49.
[69] G.K. Wertheim, M.A. Butler, K.W. West, D.N.E. Buchanan, Determination of the Gaussian and Lorentzian content of experimental line shapes, Rev. Sci. Instrum. 45 (11) (1974) 1369–1371.
[70] L. Shen, N. Wang, Effect of nitrogen pressure on the structure of Cr-N, Ta-N, Mo-N, and W-N nanocrystals synthesized by arc discharge, J. Nanomater. 2011 (2011).
[71] P. Zaumseil, High-resolution characterization of the forbidden Si 200 and Si 222 reflections, J. Appl. Crystallogr. 48 (2015) 528–532.
[72] U. Holzwarth, N. Gibson, The Scherrer equation versus the 'Debye-Scherrer equation&apos, Nat. Publ. Gr. 6 (9) (2011) 534.
[73] J.I. Langford, A.J.C. Wilson, Scherrer after sixty years: a survey and some new results in the determination of crystallite size, J. Appl. Crystallogr. 11 (2) (1978) 102–113.
[74] J.A. Thornton, Substrate heating in cylindrical magnetron sputtering, Thin Solid Films 54 (1) (1978) 23–31.
[75] J.L. Thornton, A. John, Lamb, Substrate heating rate for planar and cylindrical-post magnetron sputtering sources, Thin Solid Films 119 (1984) 87–95.
[76] J.R. Woodworth, M.E. Riley, D.C. Meister, B.P. Aragon, M.S. Le, H.H. Sawin, Ion energy and angular distributions in inductively coupled radio frequency discharges in argon, J. Appl. Phys. 80 (3) (1996) 1304–1311.
[77] T.P. Drüsedau, T. Bock, T.-M. John, F. Klabunde, W. Eckstein, Energy transfer into the growing film during sputter deposition: an investigation by calorimetric measurements and Monte Carlo simulations, J. Vac. Sci. Technol. A Vacuum, Surfaces, Film. 17 (5) (1999) 2896–2905.
[78] H. Kersten, H. Deutsch, H. Steffen, G.M.W. Kroesen, R. Hippler, The energy balance at substrate surfaces during plasma processing, Vacuum 63 (3) (2001) 385–431.
[79] A. Thomann, et al., Energy flux measurements during magnetron sputter deposition processes, Surf. Coat. Technol. 377 (2019) 1–14.
[80] S. Gauter, F. Haase, H. Kersten, Experimentally unraveling the energy flux originating from a DC magnetron sputtering source, Thin Solid Films 669 (May 2018) (2019) 8–18.
[81] P. Cormier, et al., Measuring the energy flux at the substrate position during magnetron sputter deposition processes, J. Appl. Phys. 113 (013305) (2013) 1–8.